Nuclear Engineering and Technology 58 (2026) 104208

Contents lists available at ScienceDirect

Nuclear Engineering and Technology

journal homepage: www.elsevier.com/locate/net

Original Article

CdSe/CdZnS core/shell nanocrystal scintillators: Light yield, decay time, and solvent effects

Jihwan Boo [a], Byong Jae Kim [b], Nam Young Kim [c], Ill-hyuk Han [a], Soobin Lim [d], Jaehoon Lim [b,e,f,g,*], Geehyun Kim [a,h,i,**]

[a] Department of Energy Systems Engineering, Seoul National University, Seoul, 08826, Republic of Korea
[b] Department of Energy Science, Center for Artificial Atoms, Sungkyunkwan University (SKKU), Suwon, Gyeonggi-do, 16419, Republic of Korea
[c] Department of Radiation Oncology, Yonsei Cancer Center, Seoul, 03722, Republic of Korea
[d] Q-beam Solution Inc., Daejeon, 34368, Republic of Korea
[e] Department of Energy Science, Center for Artificial Atoms, SKKU Institute of Energy Science and Technology (SIEST), Sungkyunkwan University, Gyeonggi-do, 16419, Republic of Korea
[f] Department of Future Energy Engineering, Sungkyunkwan University, Suwon, Gyeonggi-do, 16419, Republic of Korea
[g] Department of Display Engineering, Sungkyunkwan University, Suwon, Gyeonggi-do, 16419, Republic of Korea
[h] Department of Nuclear Engineering, Seoul National University, Seoul, 08826, Republic of Korea
[i] Institute of Engineering Research, Seoul National University, Seoul, 08826, Republic of Korea

ARTICLE INFO

Keywords:
Nanocrystal
Scintillator
Light yield
Decay time
Gamma ray spectroscopy

ABSTRACT

Semiconductor nanocrystals (NCs) have emerged as promising candidates for next-generation scintillators owing to their tunable band gaps and high photoluminescence quantum yields (PLQYs). However, most NC-based scintillators rely on polymer or solvent matrices, in which inefficient energy transfer and self-absorption significantly limit their light yield. In this study, we developed solvent- and polymer-free CdSe/CdZnS NC films (50–200 μm thick) and quantitatively evaluated their γ-ray response and its light yield through single-photoelectron (SPE)-based measurements. The NC films preserved their intrinsic optical characteristics after fabrication and exhibited distinct photopeaks at 59.5 keV (^{241}Am) and 81.0 keV (^{133}Ba), achieving a light yield of approximately 3200 ± 100 photons/MeV with a fast decay time of ~20 ns—comparable to reported NC/polymer nanocomposite scintillators. We further investigated solvent effects using NC-doped liquid scintillators, revealing the importance of solvent selection for observing measurable scintillation signals.

1. Introduction

Radiation detectors are essential in applications such as radioactive contamination monitoring [1–3], nuclear fuel management [4,5], and non-destructive assay of nuclear materials [6,7]. Conventional scintillators are typically based on wide-bandgap insulators ($E_g > 5$ eV), which limit the number of charge carriers generated per absorbed γ-ray energy [8]. In contrast, semiconductor nanocrystals (NCs) with narrower band gaps (2–3 eV) can produce higher carrier densities under ionizing radiation, and their emission wavelengths are tunable via size control or activator doping for precise matching to the spectral sensitivity of photosensors [9]. Core–shell structures (e.g., CdSe/CdZnS) further suppress nonradiative recombination and spatially confine electrons and holes in the core (CdSe in this case), enhancing the photoluminescence quantum yield (PLQY) [10–12]. These advantages have driven extensive research into NC-based scintillators over the past decade.

In polymer-based nanocomposite (2–20 mm thick) scintillators, photopeaks from ^{241}Am, ^{57}Co, and ^{137}Cs gamma-ray sources have been resolved, supporting their feasibility for γ-ray spectroscopy [9]. However, their thickness should be optimized to balance self-absorption–induced transmittance loss and γ-ray stopping power. Indeed, a prior study reported that increasing the scintillator thickness by threefold (from 2 to 6 mm) led to a decrease in light yield from 7,380 to 6,380 photons/MeV for nanocomposites containing 15.8 wt% nanoparticles, which was attributed to increased transmission loss due to the longer optical path length in thicker samples [13]. In such

* Corresponding author. Department of Energy Science, Center for Artificial Atoms, Sungkyunkwan University (SKKU), Suwon, Gyeonggi-do, 16419, Republic of Korea.
** Corresponding author. Department of Nuclear Engineering, Seoul National University, Seoul, 08826, Republic of Korea.
E-mail addresses: j.lim@skku.edu (J. Lim), gk.rs@snu.ac.kr (G. Kim).

https://doi.org/10.1016/j.net.2026.104208
Received 23 November 2025; Received in revised form 30 January 2026; Accepted 19 February 2026
Available online 19 February 2026

nanocomposites, even with high NC loadings (≤60 wt%), the actual NC volume fraction rarely exceeds ~20% [14], limiting the probability that excited polymer molecules are close enough to NCs to transfer energy. As a result, most absorbed energy is lost within the polymeric host, yielding only 3,000–12,000 photons/MeV—comparable to pristine polymers (~10,000 photons/MeV). Attempts to circumvent inefficient matrix-to-NC energy transfer by employing ultra-wide-bandgap inorganic NCs ($E_g > 5$ eV) have often led to reduced light yield with increased NC loading, due to their higher charge-trap densities [15]. Similarly, introducing such NCs to liquid scintillators decreased the light yield relative to the neat solvent [16]. Prior work on NC-doped liquids frequently treated the solvent as optically neutral, but solvent fluorescence, path-length-dependent visible photon loss, and refractive-index mismatch can strongly influence the light yield and obscure γ-ray spectral features [17].

In most prior studies, light yield has been evaluated relatively by comparing the Compton-edge position with that of a reference scintillator (e.g., EJ-212, assumed to produce 10,000 photons/MeV with little variability). In practice, assigning the Compton edge for each scintillator is nontrivial, because its apparent position depends on scintillator type, geometry, and the incident γ-ray energy; robust determination typically requires Compton-coincidence methods or Monte Carlo–guided spectral fitting [18,19]. Uncertainty in the edge position propagates into relative light-yield estimates, energy calibration, and non-proportionality analysis. These considerations motivate the use of absolute light-yield measurements.

In this study, we developed solvent- and polymer-free CdSe/CdZnS NC films (50–200 μm thick) designed to minimize self-absorption while maintaining sufficient γ-ray interaction probability. Their light yield was quantified via an absolute single-photoelectron-based measurement, and the effect of solvent environment was further examined using NC-doped liquid scintillators. This approach establishes a new solid-state nanoscintillator platform capable of resolving low-energy γ peaks and enabling quantitative light-yield measurement.

2. Methods

2.1. Synthesis of CdSe/CdZnS core/shell NCs

CdSe/CdZnS core/shell NCs were synthesized via a one-pot successive growth approach, as described in our previous work [11]. Briefly, a mixture of 1 mmol CdO, 3 mmol myristic acid, and 15 mL 1-octadecene was heated to 300 °C under inert conditions. At this temperature, 0.25 mL of 2 M trioctylphosphine selenide (TOP-Se) was rapidly injected to initiate CdSe core nucleation. After 3 min, 3 mL of 0.5 M zinc oleate and 1-dodecanethiol were added dropwise to begin CdZnS shell formation. The reaction continued for 30 min, followed by the addition of 2 mL of 0.5 M cadmium oleate, 4 mL of 0.5 M zinc oleate, and 1.5 mL of 2 M trioctylphosphine sulfide (TOPS) to complete shell growth. The resulting NCs were purified five times using ethanol and redispersed in toluene or hexane.

2.2. Fabrication of NC film scintillators

Fig. 1 illustrates the fabrication of CdSe/CdZnS NC films (diameter: 6 mm; thickness: 50–200 μm) on a glass substrate using photolithography and deep wet etching [20]. A 30 nm chromium (Cr) layer was first deposited on a 500 μm thick glass wafer, followed by 200 nm of gold (Au) deposition. A photoresist (AZ4330) was spin-coated, patterned by UV exposure, and developed. The exposed Cr/Au layers were etched to reveal the glass surface, and another Cr/Au layer was deposited on the wafer's backside.

The patterned wafer was immersed in buffered oxide etchant (BOE, $HF:NH_4F = 1:3$), and the etch depth (up to 200 μm) was controlled by immersion time. After etching, the remaining metal layers were removed. A 50 nm thick aluminum layer (91% reflectance at 630 nm) was deposited on the substrate using a thermal evaporator installed in a glove box. The NC solution was drop-cast into the groove in the glove box, with the groove depth determining the film thickness. Finally, a 100 μm-thick Corning Willow glass layer (83% transmittance at 630 nm) was placed over the film to protect against air and moisture while transmitting light to a light sensor, such as a photomultiplier tube (PMT).

To evaluate energy deposition by ionizing radiation, we conducted Monte Carlo simulations using an NC superlattice geometry representative of the NC films, as shown in Fig. 2. Because the ranges of secondary electrons generated by γ-ray interactions commonly extend well beyond the ~10 nm scale of individual nanocrystals [21], we adopted a mesoscale modelling approach. Specifically, we constructed a periodic lattice model of spherical CdSe/CdZnS NCs (radius: 6.5 nm; CdSe core: 2.0 nm; shell: 4.5 nm, as determined in our previous study [11]) within a film with a total thickness of 50–200 μm. We assumed that interstitial regions were filled with surface ligands.

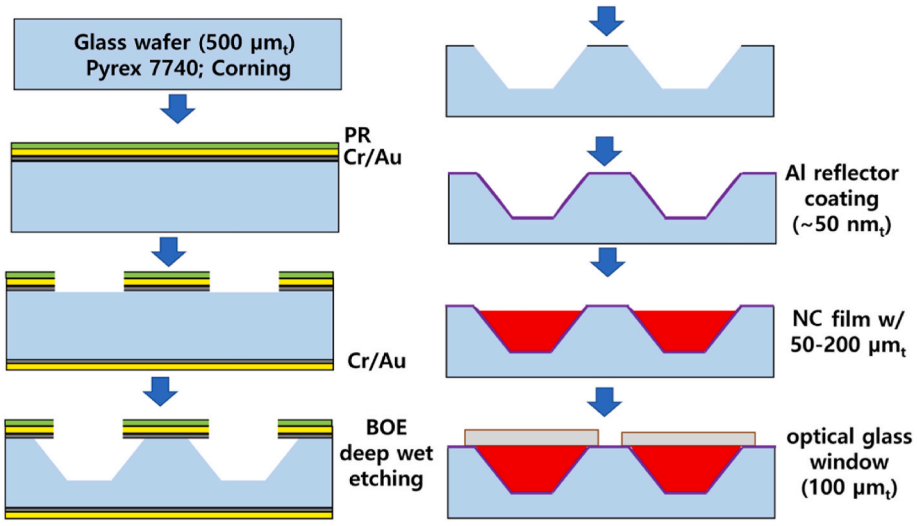

Fig. 1. Schematic illustration of the fabrication of a CdSe/CdZnS NC film with a thickness of a few hundred microns on a glass wafer using a photolithographic process.

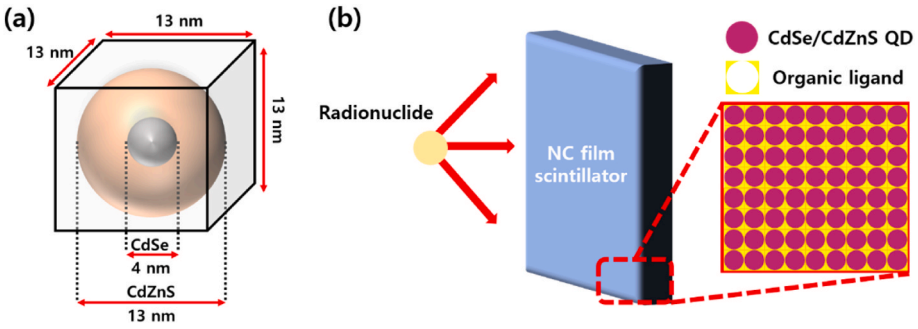

Fig. 2. (a) The geometric structure of CdSe/CdZnS NC and (b) the schematic of the simulation geometry of the NC film with a thickness of several hundred micrometers by repeating the NC thousands of times.

2.3. Fabrication of NC-doped liquid scintillators

Taking advantage of the high PLQY of the CdSe/CdZnS nanocrystals (87%; Fig. S1), the as-synthesized colloidal solution was directly employed as a liquid scintillator to investigate the effect of different solvents on scintillation performance. The NC colloidal solution was loaded into quartz cuvettes (diameter: 22 mm, optical path length: 1 mm), as shown in Fig. 3(a). Due to the thick cuvette neck, optical coupling to the photomultiplier tube (PMT) was achieved through a 2.5 mm-thick quartz window. In addition, a 10 mm path-length cuvette was employed to investigate the effect of increased optical path length on scintillation characteristics and light output.

As illustrated in Fig. 3(b), gamma-rays interact with the high-Z Cd atoms in the NCs, producing primary electrons that, in turn, generate numerous secondary electrons through Coulomb scattering with nearby NCs or solvent molecules. These secondary processes result in local excitation and ionization events within the liquid medium. Subsequently, as depicted in Fig. 3(c and d), the generated excitons in the NCs or solvent molecules can transfer energy radiatively or non-radiatively (e.g., via Förster resonance energy transfer, FRET) to the NCs, leading to visible light emission. Hexane (PLQY <0.001) was selected as a low-background solvent, while toluene (PLQY = 0.17) was used for comparison to assess solvent-induced variations in light output.

2.4. Light yield measurement via single-photoelectron analysis

Light yield measurement using the single-photoelectron (SPE) method is based on the proportionality between light yield and the number of photoelectrons generated in a photodetector. Fig. 4 illustrates the experimental setup for measuring SPE by detecting the minimum output current generated by the PMT (R2228, Hamamatsu) upon photon incidence, following the protocol reported in our previous work [22]. A pulse generator sent electrical pulses (100 Hz, 8 ns width) to an LED and simultaneously provided trigger signals to a high-speed digitizer (DT5730, 500 MS/s, 14-bit). The PMT output was recorded using a leading-edge trigger synchronized with the LED trigger, allowing event capture within a 140 ns time window. Events exhibiting a distinct temporal correlation within the predefined time window were used as true coincidence events. The total charge of each PMT pulse, hereinafter referred to as the integrated charge, was calculated by summing the waveform amplitude over all sampling points.

Light yield can be defined either as absolute or technical light yield [22]. The absolute LY is the ratio of the number of scintillation photons generated per MeV, while the technical LY is that of experimentally

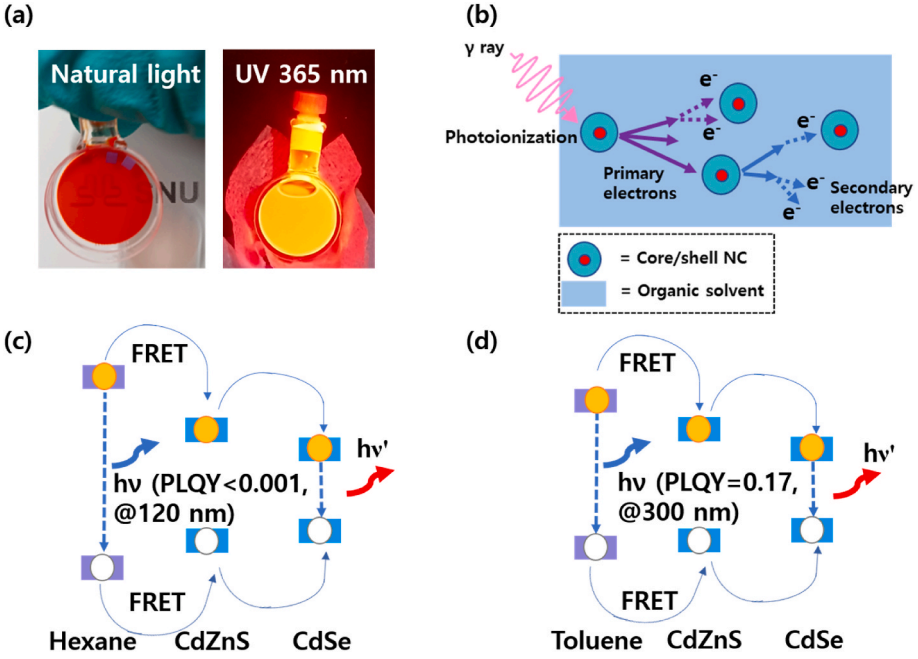

Fig. 3. (a) Photographs of NC-doped liquid scintillators under natural and UV light, and schematic representation of energy deposition and scintillation mechanisms in NC-doped liquid scintillators: (b) gamma ray energy deposition through electron cascades, and (c,d) energy-transfer pathways in hexane- and toluene-based scintillators.

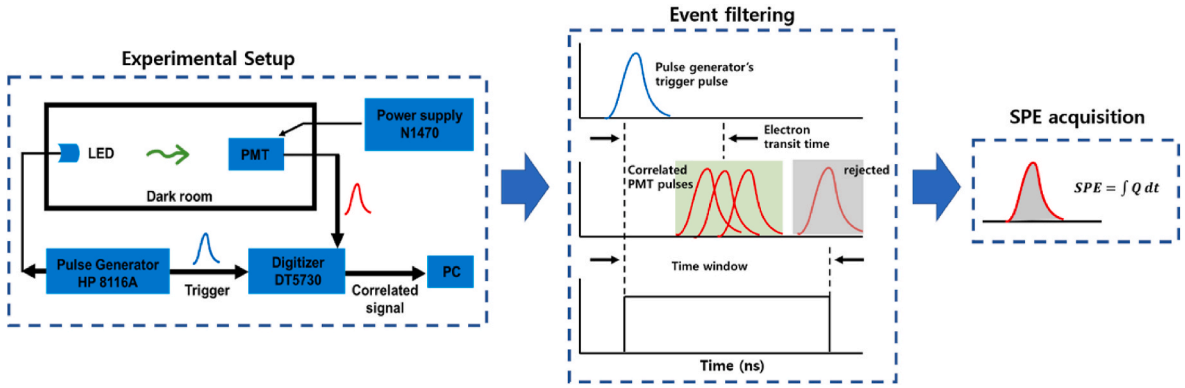

Fig. 4. A schematic of the experimental setup for measuring SPE.

measured scintillation photons passing through the entrance window of the scintillator per MeV. The two quantities are related by the light collection efficiency (LCE), which accounts for photon losses arising from internal trapping within the scintillator and imperfect surface reflections. Although LCE can, in principle, be estimated, simulation-based evaluations are often unreliable [23,24]. In this study, we therefore focused on the technical light yield, assuming LCE of unity and thereby excluding optical collection losses from the analysis.

The light yield was determined by comparing the integrated charge generated by a known radiation energy (e.g., 59.5 keV γ rays from ^{241}Am) with that of the SPE response, according to Equation (1).

$$T_{LY} \approx \frac{IC_{241_{Am}}}{IC_{SPE}} \times \frac{1}{0.05954} \times \frac{1}{\overline{QE}} \times \frac{1}{LCE} \quad (1)$$

Where T_{LY}, $IC_{241_{Am}}$, and IC_{SPE} refer to the technical light yield, the integrated charge measured from 59.54 keV gamma-rays emitted by ^{241}Am and from a SPE pulse, respectively. $\overline{QE}$ is the effective quantum efficiency by convolving the scintillator's emission spectrum with the R2228 PMT's spectral response (see Fig. S1). We applied optical grease (BC630, Saint-Gobain) at the PMT-scintillator interface for optical coupling. This reduced reflection losses at the PMT window, which would otherwise have an 8% loss due to the refractive index of glass (approximately 1.5) [23]. Considering this, the $\overline{QE}$ was estimated to be 7.7%.

Fig. 5(a) shows the γ-ray measurement setup, which employed a digitizer-based configuration to quantify the light yield under identical measurement conditions. The digitizer directly acquired the PMT anode output without a preamplifier or a shaping amplifier. The PMT output was recorded when the signal amplitude exceeded the trigger threshold, as illustrated in Fig. 5(b). The baseline was corrected by subtracting the mean signal level measured within the baseline gate, and the waveform was then integrated over a 360 ns gate—enough to collect the full charge corresponding to the NC scintillator decay time (30–60 ns). The resulting integrated charge represented the total charge of each PMT pulse, which was proportional to the energy deposited by the incident γ ray.

3. Results and discussion

3.1. Optical properties of CdSe/CdZnS NC films

Fig. 6(a) shows the side view of the etched glass substrate observed by a scanning electron microscope (SEM). The groove has a gentle slope of approximately 168°, which is favorable for reflector coating. Fig. 6(b) displays the NC films formed on the groove of various depths, ranging from 50 μm to 200 μm. To investigate the optical properties, we performed steady-state and time-resolved photoluminescence (PL) measurements using a spectrofluorometer (Fluoromax Plus, Horiba) under the core-only excitation condition (excitation wavelength: 450 nm) to exclude the carrier excitation in the shell layer [11]. The as-synthesized CdSe/CdZnS NC colloidal solution exhibited a PL peak centered at ~630 nm (Fig. S1), arising from band-edge (exciton) emission in the CdSe core, that is, radiative electron–hole recombination between conduction-band electrons and valence-band holes. Also, the fabricated NC films maintained a consistent emission peak at ~630 nm regardless of thickness, as shown in Fig. 6(c), indicating that the optical properties were preserved throughout the fabrication process. For thicker films, an additional spectral feature appeared in the 650–725 nm region. To identify its origin, we conducted angle-dependent PL measurements by tilting the films (Fig. S3). The location and prominence of this long-wavelength feature vary strongly with tilt angle, and the effect becomes more pronounced for the 200-μm film. This pronounced angle dependence is largely attributed to interference effects arising from the coherent superposition of emitted and internally reflected luminescence [25], whose spectral modulation depends sensitively on the film thickness and reflectivity of the glass window/film/substrate configuration. Meanwhile, the decay time increased slightly with film thickness (15.2 ns for 50 μm, 18.3 ns for 100 μm, and 20.0 ns for 200 μm), as shown in Fig. 6(d), which may reflect additional photon-transport processes, such as reabsorption and re-emission, and/or increased optical path lengths in thicker films.

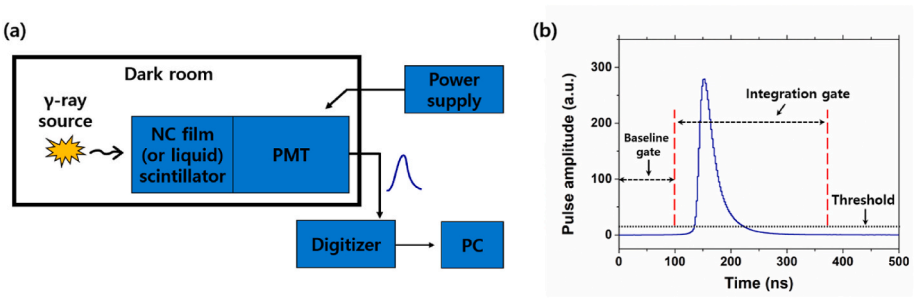

Fig. 5. (a) Schematic diagram of the gamma ray measurement setup, and (b) an example of a digitized waveform of the CdSe/CdZnS NC scintillator.

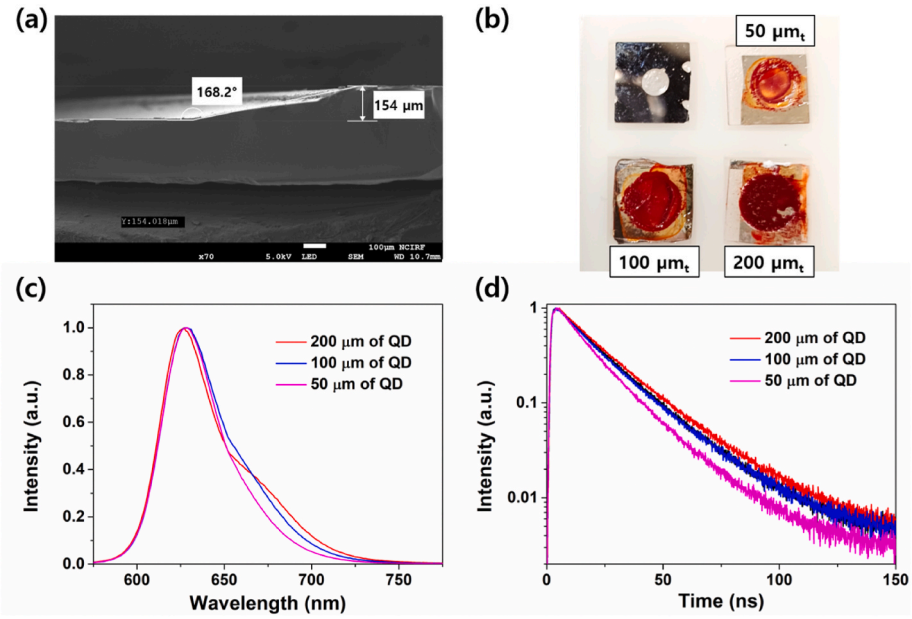

Fig. 6. (a) SEM micrograph of a cross-section of the glass-based substrate and (b) a photograph of the representative NC scintillator film with a different thickness on the substrate. (c) PL emission spectra and (d) decay curves with a different thickness of NC film excited at 450 nm.

3.2. *Digitizer-based single-photoelectron (SPE) event analysis*

Fig. 7(a) shows a digitized trigger from the pulse generator and the temporally correlated PMT-anode waveform under LED excitation. The PMT response lags the trigger by the electron transit time delay ($\Delta T = t_{PMT} - t_{trig}$), typically ~60 ns for the R2228, with additional delay arising from cable length and front-end electronics. To select true coincidences, we plotted a two-dimensional distribution of integrated PMT signal charge versus the ΔT, and events within the 68–100 ns window were accepted as true coincidence events, as indicated in Fig. 7(b). Fig. 7(c) presents the integrated charge distributions corresponding to SPE and double-photoelectron (DPE) responses. The peak near zero charge arises from background (BKG) signals, whereas the DPE peak appears at approximately twice the SPE charge. We deconvolved the spectrum by fitting a superposition of three Gaussians (BKG, SPE, DPE), as described in Ref. [22]. The SPE centroid was 251.8 ± 3.9 (a.u.). In our recent preliminary study [22], eliminating random coincidences originating from dark counts and baseline fluctuations yields a clearly resolved SPE

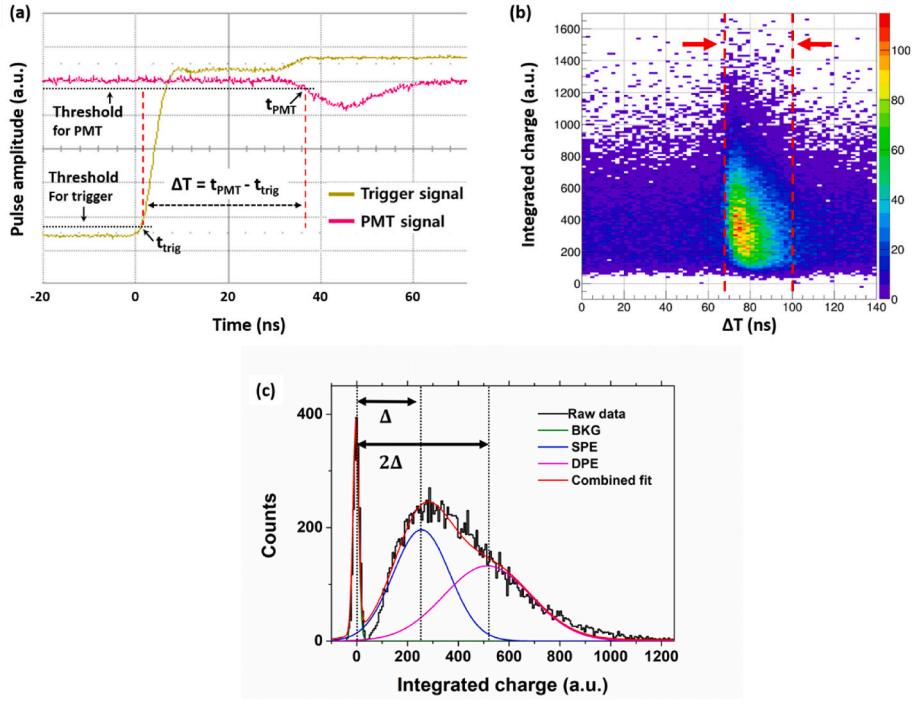

Fig. 7. (a) Example of digitized waveforms; the pulse-generator trigger and the time-correlated PMT anode response under LED excitation. (b) Two-dimensional distribution of integrated charge for PMT signal versus arrival-time difference (ΔT) between trigger and PMT signal at low light intensity; the highlighted time window (68–100 ns) denotes the region used to select true-coincidence events. (c) Corresponding integrated-charge spectra of the PMT anode output under LED excitation.

distribution compared with the classic self-triggering approach (which records all PMT signals exceeding the threshold without temporal correlation to the LED trigger). These preliminary findings suggested that selecting true coincidence events for analysis yielded a more accurate estimation of SPE charge and, consequently, light yield. This observation served as the experimental basis for the present study.

3.3. Gamma ray response and light yield measurement in NC films

We evaluated the gamma ray response and light yield of CdSe/CdZnS NC films deposited on Al-coated glass substrates. To ensure accurate light-yield evaluation and remove radiation-induced background signals originating from the PMT and glass substrate, we obtained net spectra by subtracting the spectrum of a neat glass substrate from that of the NC-coated glass; both were measured under identical ^{241}Am γ-ray irradiation and acquisition conditions. Fig. 8(a) presents the ^{241}Am spectra measured from NC films of varying thicknesses (50, 100, and 200 μm). All samples exhibited a single photopeak at an integrated charge of 3,710 ± 10 (a.u.), and the count rate increased with increasing film thickness, indicating enhanced detection efficiency due to a greater probability of gamma ray interaction. MCNP simulations in Fig. 8(b) corroborate that energy deposition occurs predominantly via the photoelectric effect, yielding a full-energy absorption peak at 59.5 keV for all thicknesses.

We used the SPE charge as the reference for one photoelectron. The number of photoelectrons was determined from the ratio of the mean charge of the 59.5 keV photopeak (3,710 a.u.) to the mean SPE charge (251.8 a.u.) and then normalized by 59.5 keV (0.0595 MeV), yielding 247 ± 4 photoelectrons/MeV. From repeated measurements of SPE (four runs) and ^{241}Am spectra (five runs), the light yield of the NC films was determined to be 3,200 ± 100 photons/MeV, comparable to values reported for NC/polymer nanocomposite scintillators (e.g., 2,440 photons/MeV for 58.9 wt% YbF_3) [26]. This modest scintillation light yield is primarily limited by the reduced radiative efficiency of the NC films. Supporting this, the absolute PLQY decreased substantially upon film formation, from 84.0 ± 3.0% in colloidal solution to 16.1 ± 3.0% (50 μm), 13.3 ± 3.0% (100 μm), and 15.6 ± 3.0% (200 μm) for the solid films, as measured using an integrating sphere (Fig. S4). Such PLQY reduction in NC solids is commonly attributed to the activation of fast nonradiative pathways and exciton migration via inter-NC energy transfer, during which excitations can be quenched at nonradiative sites [27]. A similar PLQY decrease upon film formation was also observed in our previous work [11]. Nevertheless, the NC films consistently resolved the 59.5 keV photopeak across 50–200 μm thicknesses and achieved an absolute light yield comparable to representative NC/polymer nanocomposites.

Fig. 8(c) shows the net gamma ray spectrum of the 200 μm thick NC film under ^{133}Ba irradiation. We observed a full energy absorption peak corresponding to the 81.0 keV gamma ray at an integrated charge of 4,540 ± 30 (a.u.) along with the characteristic $K_{\alpha,\beta}$ X-ray peak (30–35 keV). These features were consistent with the MCNP simulation in Fig. 8 (d). In contrast, no full-energy absorption peak was observed for higher-energy γ rays such as the 662 keV γ rays from ^{137}Cs, due to the limited film thickness. These results demonstrate that few-hundred-micrometer NC films can resolve photopeaks in the tens-of-keV range and enable quantitative light-yield measurements.

3.4. Optical properties and gamma ray response in NC-doped liquid scintillators

We investigated how optical path length affects the PL characteristics of CdSe/CdZnS NC-doped liquid scintillators. As shown in Fig. 9(a) and (b), NCs dispersed in hexane (0.5–6 wt%) in a cuvette with a 1 mm optical path exhibited a slight redshift in PL emission from 624 nm to 630 nm, accompanied by an increase in decay time from 26.2 ns to 44.9 ns. These results indicate a concentration-dependent emission behavior, where higher NC loadings enhance photon reabsorption followed by red-shifted re-emission.

When the optical path length increased to 10 mm, the PL peak shifted more substantially from 626 nm to 667 nm at NC loadings of 0.5–6 wt% (see Fig. S2) and the decay time was prolonged from 42.6 ns to 110.8 ns. This pronounced redshift led to a spectral mismatch with the PMT's maximum sensitivity near 600 nm, thereby reducing detection efficiency. These results suggest that a shorter optical path (1 mm)

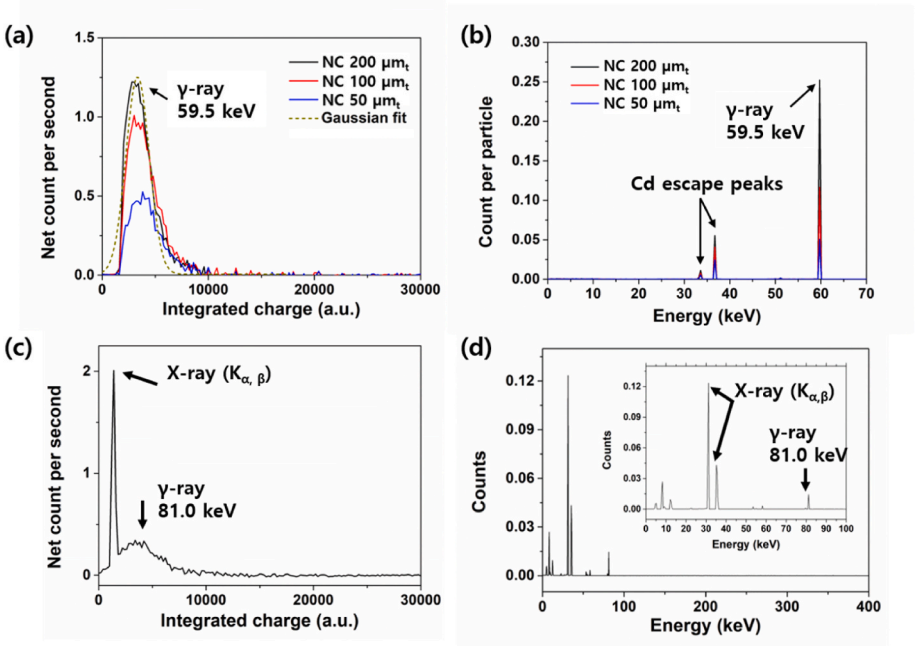

Fig. 8. Experimental γ-ray spectra of CdSe/CdZnS NC films with different thicknesses (50, 100, and 200 μm) under ^{241}Am gamma ray irradiation, and (b) the corresponding MCNP-simulated energy deposition spectra, confirming a 59.5 keV full-energy peak dominated by the photoelectric effect. (c) Experimental γ-ray spectrum of a 200 μm NC film under ^{133}Ba irradiation, and (d) the corresponding MCNP-simulated energy deposition spectrum.

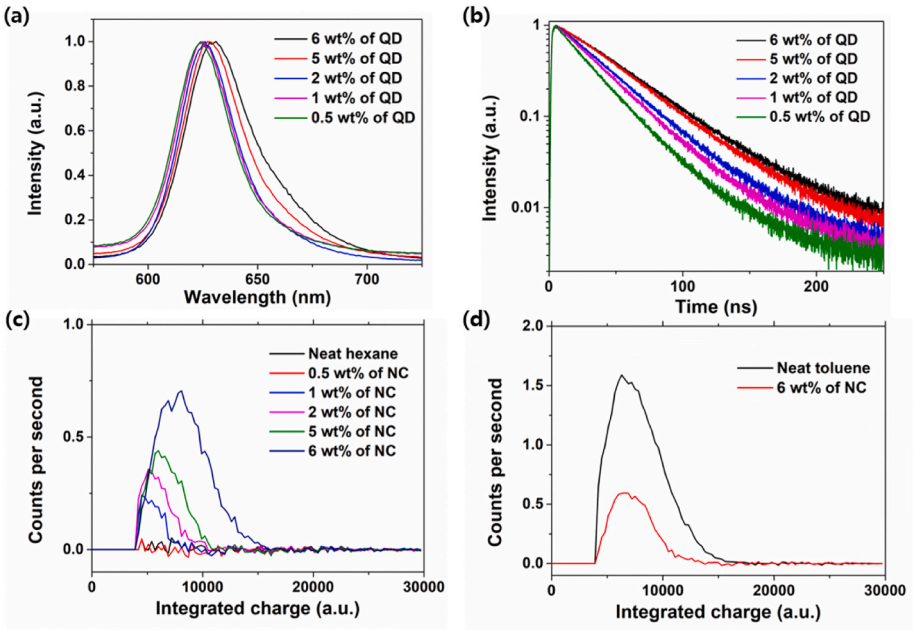

Fig. 9. (a) PL emission spectra (excitation at 450 nm) and (b) decay profiles of CdSe/CdZnS NC-doped hexane at various NC loadings (0.5-6 wt%), measured in a 1 mm optical-path cuvette. (c) Net gamma spectra of NC-doped hexane and (d) NC-doped toluene (at 6 wt% NC) under ^{137}Cs gamma ray irradiation.

effectively minimizes reabsorption and provides more reliable conditions for γ-ray response measurements.

We further examined how NC concentration and the solvent environment affect the γ-ray response of NC-doped liquid scintillators. Net gamma spectra were obtained by subtracting the spectrum of an empty vial from that of NC-doped hexane acquired under identical ^{137}Cs irradiation and acquisition settings. As shown in Fig. 9(c), increasing NC loading in hexane shifted the peak centroid in integrated charge from 5,350, 5,720, 6,570, and 8,010 (a.u.) for NC concentrations of 1 wt%, 2 wt%, 5 wt%, and 6 wt%, respectively, demonstrating increased light yield with higher NC concentration. This behavior is expected because higher NC loading provides more emissive centers that can be directly excited by secondary electrons and places more NCs in the vicinity of excited solvent molecules, thereby enhancing the probability of non-radiative energy transfer (e.g., FRET) to the NCs.

In the NC-doped liquid scintillator, however, the medium is dominated by an organic solvent and the NC volume fraction is small. Consequently, γ rays from ^{137}Cs interact predominantly via Compton scattering within the solvent, and only a small fraction of the deposited energy is transferred to the NCs. The resulting number of photoelectrons per event is therefore insufficient to resolve spectral features, which precludes quantitative light yield analysis and similarly suppresses peak formation for lower-energy γ sources such as ^{241}Am.

Unlike hexane, NC-doped toluene (6 wt%) exhibited a substantially reduced gamma ray response compared with neat toluene. As shown in Fig. 9(d), although toluene produces strong intrinsic fluorescence under ^{137}Cs irradiation, much of this solvent-originated emission is reabsorbed by the NCs and, due to their finite PLQY, is not fully re-emitted, resulting in fewer photons reaching the PMT. Consequently, the recorded count rate was markedly reduced in NC-doped toluene. Overall, these results confirm that hexane, with its lower intrinsic fluorescence, enables a more accurate evaluation of NC-originated scintillation by minimizing solvent-induced radiative interference.

4. Conclusions

In this study, we developed solvent- and polymer-free CdSe/CdZnS nanocrystal (NC) films and investigated their optical and γ-ray scintillation properties through absolute light-yield measurements. The NC films preserved their intrinsic PL characteristics during fabrication, and few-hundred-micrometer-thick films could resolve photopeaks in the tens-of-keV range. The decay time and light yield were estimated to be ~20 ns and 3,200 ± 100 photons/MeV, respectively, using SPE-based light-yield measurement. This performance is comparable to previously reported NC/polymer nanocomposite scintillators, despite the absence of a polymer matrix, demonstrating the feasibility of NC films as solid-state NC scintillators.

In parallel, the influence of the solvent environment on NC-doped liquid scintillators was examined. NC-doped hexane provided measurable scintillation responses, whereas NC-doped toluene showed a substantial reduction in detectable signal. Although toluene generates strong intrinsic fluorescence under γ-ray irradiation, much of this solvent-originated emission is reabsorbed by the NCs, resulting in markedly suppressed scintillation signals. These findings highlight that solvent choice critically affects the interpretation of NC-originated scintillation in NC-doped liquid scintillators. Overall, this study establishes a framework for quantitative evaluation of NC scintillators and highlights the potential of solvent-free NC films as a compact platform for γ-ray detection and future NC scintillator optimization.

CRediT authorship contribution statement

Jihwan Boo: Writing – original draft, Visualization, Validation, Methodology, Investigation, Formal analysis, Data curation, Conceptualization. **Byong Jae Kim:** Writing – review & editing, Methodology, Investigation, Formal analysis, Data curation. **Nam Young Kim:** Writing – review & editing, Methodology, Investigation, Formal analysis, Data curation, Conceptualization. **Ill-hyuk Han:** Writing – review & editing, Software. **Soobin Lim:** Writing – review & editing, Resources. **Jaehoon Lim:** Writing – review & editing, Resources. **Geehyun Kim:** Writing – review & editing, Supervision, Resources, Project administration, Funding acquisition.

Declaration of competing interest

The authors declare that they have no known competing financial interests or personal relationships that could have appeared to influence the work reported in this paper.

Acknowledgments

This work was supported by National Research Foundation of Korea (NRF) funded by the Ministry of Science and ICT (2022M2D2A1A02063826).

Appendix A. Supplementary data

Supplementary data to this article can be found online at https://doi.org/10.1016/j.net.2026.104208.

Data availability

Data will be made available on request.

References

[1] K. Vetter, R. Barnowksi, A. Haefner, T.H. Joshi, R. Pavlovsky, B.J. Quiter, Gamma-ray imaging for nuclear security and safety: towards 3-D gamma-ray vision, Nucl. Instrum. Methods Phys. Res. Sect. A Accel. Spectrom. Detect. Assoc. Equip. 878 (2018) 159–168.

[2] M. Jeong, B. Van, B.T. Wells, L.J. D'Aries, M.D. Hammig, Scalable gamma-ray camera for wide-area search based on silicon photomultipliers array, Rev. Sci. Instrum. 89 (2018) 033106.

[3] H.S. Kim, G. Kim, S.J. Ye, Dual-particle imaging performance of a Cs_2LiYCl_6:Ce (CLYC)-based rotational modulation collimator (RMC) system, IEEE Trans. Nucl. Sci. 69 (2021) 1389–1396.

[4] C. Willman, A. Håkansson, O. Osifo, A. Bäcklin, S.J. Svärd, Nondestructive assay of spent nuclear fuel with gamma-ray spectroscopy, Ann. Nucl. Energy 33 (2006) 427–438.

[5] W. Hong, G. Kim, A monte carlo simulation study for designing collimators for a CZT-based spent nuclear fuel characterization system, Nucl. Instrum. Methods Phys. Res. 1064 (2024) 169332.

[6] D. Reilly, N. Ensslin, H. Smith Jr., S. Kreiner, Passive Nondestructive Assay of Nuclear Materials, Office of Nuclear Regulatory Research; Los Alamos National Laboratory (LANL), Los Alamos, NM (United States), 1991. No. NUREG/CR-5550; LA-UR-90-732. US Nuclear Regulatory Commission (NRC), Washington, DC (United States).

[7] J. Jeon, C.J. Park, G. Kim, A characterization method for reprocessed spent nuclear fuel through neutron and gamma-ray multiplicity counting, Nucl. Eng. Technol. 57 (2025) 103232.

[8] B.D. Milbrath, A.J. Peurrung, M. Bliss, W.J. Weber, Radiation detector materials: an overview, J. Mater. Res. 23 (2008) 2561–2581.

[9] J. Boo, I.H. Han, G. Kim, Nanocomposite radiation detectors for gamma-ray spectroscopy, J. Radiation Protect. Res. 50 (2025) 63–90.

[10] P. Reiss, M. Protiere, L. Li, Core/shell semiconductor nanocrystals, Small 5 (2009) 154–168.

[11] J. Lim, B.G. Jeong, M. Park, J.K. Kim, J.M. Pietryga, Y.S. Park, et al., Influence of shell thickness on the performance of light-emitting devices based on $CdSe/Zn_{1-x}Cd_xS$ core/shell heterostructured quantum dots, Adv. Mater. 26 (2014) 8034–8040.

[12] J. Lim, Y.S. Park, V.I. Klimov, Optical gain in colloidal quantum dots achieved with direct-current electrical pumping, Nat. Mater. 17 (2018) 42–49.

[13] Y. Chen, C. Liu, Y. Jin, T.J. Hajagos, D. Kishpaugh, Q. Zhuang, et al., Ytterbium fluoride loaded plastic scintillators for γ-ray spectroscopy, in: R.B. James, M. Fiederle, A. Burger (Eds.), Hard X-ray, gamma-ray, and Neutron Detector Physics XVIII, 9968 Proc SPIE, 2016.

[14] D.A. Vecchio, D.H. Mark, A.K. Nicholas, High-resolution radiation sensors from flexible network nanocomposites of nanoparticles and aramid nanofibers, ACS Nano 19 (2025) 11924–11935.

[15] C. Liu, T.J. Hajagos, D. Kishpaugh, Y. Jin, W. Hu, Q. Chen, et al., Facile single-precursor synthesis and surface modification of hafnium oxide nanoparticles for nanocomposite γ-ray scintillators, Adv. Funct. Mater. 25 (2015) 4607–4616.

[16] H. Zhao, H. Yu, C. Redding, Z. Li, T. Chen, Y. Meng, et al., Scintillation liquids loaded with hafnium oxide nanoparticles for spectral resolution of γ rays, ACS Appl. Nano Mater. 4 (2021) 1220–1227.

[17] T.J. Hajagos, C. Liu, N.J. Cherepy, Q. Pei, High-Z sensitized plastic scintillators: a review, Adv. Mater. 30 (2018) e1706956.

[18] L. Swiderski, M. Moszyński, W. Czarnacki, J. Iwanowska, A. Syntfeld-Każuch, T. Szczęśniak, et al., Measurement of compton edge position in low-Z scintillators, Radiat. Meas. 45 (2010) 605–607.

[19] C. Kim, J. Kim, W. Hong, J.Y. Yeom, G. Kim, Development of an energy and efficiency calibration method for stilbene scintillators, Nucl. Eng. Technol. 54 (2022) 3833–3840.

[20] A. Nigam, V. Sahu, P.K. Menon, P. Pal, Study of masking layer behavior towards bulk micromachining of borofloat glass, Mater. Today Proc. 92 (2023) 823–828.

[21] A.L. Bulin, A. Vasil'Ev, A. Belsky, D. Amans, G. Ledoux, C. Dujardin, Modelling energy deposition in nanoscintillators to predict the efficiency of the X-ray-induced photodynamic effect, Nanoscale 7 (2015) 5744–5751.

[22] J. Boo, N. Kim, G. Kim, Digitizer-based single-photoelectron detection approach for the light yield measurement of inorganic scintillators, J. Radiat. Prot. Res. (2026), https://doi.org/10.14407/jrpr.2025.00115.

[23] M. Moszynski, M. Kapusta, M. Mayhugh, D. Wolski, S.O. Flyckt, Absolute light output of scintillators, IEEE Trans. Nucl. Sci. 44 (1997) 1052–1061.

[24] N.Z. Galunov, O.A. Tarasenko, V.A. Tarasov, Determination of the light yield of organic scintillators, Function. Mater. (2013).

[25] J.K. Larsen, S.Y. Li, J.J.S. Scragg, Y. Ren, C. Hägglund, M.D. Heinemann, et al., Interference effects in photoluminescence spectra of Cu_2ZnSnS_4 and $Cu(In,Ga)Se_2$ thin films, J. Appl. Phys. 118 (2015) 035307.

[26] Y. Jin, D. Kishpaugh, C. Liu, T.J. Hajagos, Q. Chen, L. Li, et al., Partial ligand exchange as a critical approach to the synthesis of transparent ytterbium fluoride–polymer nanocomposite monoliths for gamma ray scintillation, J. Mater. Chem. C 4 (2016) 3654–3660.

[27] G.M. Akselrod, F. Prins, L.V. Poulikakos, E.M. Lee, M.C. Weidman, A.J. Mork, et al., Subdiffusive exciton transport in quantum dot solids, Nano Lett. 14 (2014) 3556–3562.